Full Length Research Paper

A multilevel fast multipole method for computing the propagation of multiply scattered 2.5-D teleseismic surface waves underneath a linear or quasi-linear seismic station array

Özcan Çakir

Nevşehir University, Department of Geophysics, 50300, Nevşehir, Turkey. E-mail: ocakir@nevsehir.edu.tr.

We introduce an algorithm for the forward modeling of multiple scattering of teleseismic surface waves where the underground structure beneath the linear (or quasi-linear) seismic station array is assumed two-dimensional and the teleseismic surface waves may be approached from an arbitrary direction. The current algorithm is two-and-half-dimensional since even though the structure is two-dimensional, the displacements are three-dimensional because of scattering outside the sagittal plane. The total displacement field is computed by applying a convolutional type integral equation for which the Green's function is obtained by employing the normal mode theory in one-dimensional reference structure. When the number of data points gets large, the wavefield computations become awkward. In order to alleviate the computational burden, we employ the proficient multilevel fast multipole method where the central processing unit (CPU) time increases logarithmically with the size of the model.

Key words: Green's function, heterogeneity, integral equation, multiple scattering, multipole expansions, surface waves.

INTRODUCTION

Numerical simulation of seismic wave propagation (both body and surface waves) is one of the major geophysical tools widely used to delineate the earth's elastodynamic structure where the basic process (that is inversion) is to seek a match between the observational and theoretical wavefields (Lebedev and van der Hilst, 2008). Depending on the target structure, a particular segment of the recorded wavefield is modeled; e.g. travel times in tomography (Schmid et al., 2008), primary reflections in reflection seismology (Laigle et al., 2008) and converted phases in receiver function modeling (Xu et al., 2007). In these modeling efforts, the main concern is to increase the resolution power of the respective simulation process for which geophysicists have developed sophisticated data acquisition systems involving multidimensional coverage such as two-and-half-dimensional (2.5-D) and three-dimensional (3-D) seismograph arrays and also sophisticated numerical algorithms capable of computing wave propagation in heterogeneous structures.

The numerical algorithms fall into several categories where the most commonly known methods are finite elements (Pain et al., 2005), finite differences (Moczo et al., 2000), spectral elements (Tromp et al., 2008), direct solution method (Cummins et al., 1997), complex-screen method (Wu et al., 2000) and boundary element method (Liu et al., 2008). Other distinctly defined methods (Faccioli et al., 1997; Fu and Bouchon, 2004; Haines et al., 2004; Gao and Zhang, 2006) also exist, which are capable of solving complex wave propagation problems. Some of these methods discretize the entire propagating medium (e.g. finite elements and finite differences) while others use diagonal mass matrix (e.g. spectral element method).

Herein we propose a 2.5-D algorithm for fast and memory efficient forward modeling of teleseismic surface waves recorded on a linear (or quasi-linear) seismograph array. This 2.5-D treatment is adequate for regions along active and passive continental margins, suture zones,
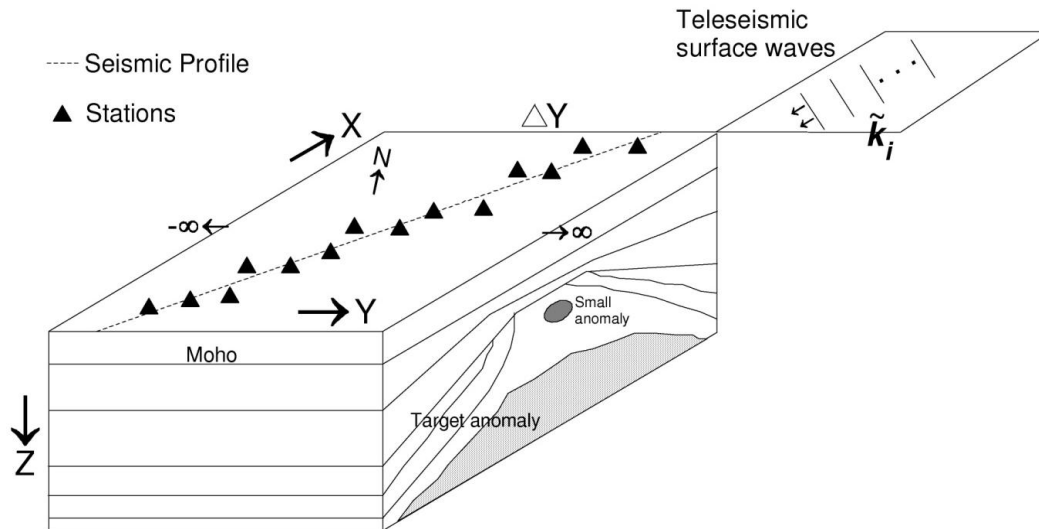
Figure 1. A simplified graphical view of the recording geometry for a 2.5-D teleseismic surface wave experiment is shown. The underground geology is assumed 2-D for a slab with width ΔY, which is theoretically realized as extending to infinity.

mountain ranges and sedimentary valleys where the earth's structural variation is mostly smooth or approximately translationally invariant, for a slab with comparable width to the observed wavelength. Figure 1 represents a simplified drawing of the 2.5-D geometry. The wavefield is mainly solved in a 1-D layered reference structure and the heterogeneities have arbitrary 2-D variations. The incident wave may arrive from an arbitrary Back Azimuth, which makes the observed waveforms 3-D in nature, which is as a result of scattering observed outside the arrival plane, and the source and receiver on the same great-circle path. Many seismic experiments conducted on quasi-linear station arrays (Zhu, 2000; Yamauchi et al., 2003; Chen et al., 2005; Wilson et al., 2005) indicate the importance of 2.5-D approach for the teleseismic surface waves.

In the proposed algorithm, we represent the total wavefield as a combination of low frequency homogeneous waves traveling in the smoothly varying background structure and high frequency heterogeneous waves created by arbitrary structural variations perturbing the background structure. Thereby heterogeneities adequately discretized are treated as secondary impulse sources in the medium, which are then coupled to the total wavefield through a convolutional integral equation. We solve the homogeneous wavefield in a one-dimensional (1-D) layered Cartesian structure overlying a half-space for which the impulse response is defined using the normal mode theory (Abo-Zena, 1979; Chen, 1993). In order to achieve the current 2.5-D surface wave algorithm, we basically modify the 3-D surface wave formulation already defined elsewhere (Takeuchi and Saito, 1972; Maupin, 2001; Çakir, 2006).

We take the advantages of the fast multipole method (FMM), which was first proposed by Rokhlin (1985) and later improved by Greengard and Rokhlin (1987). Increasingly more geophysicists (Fujiwara, 1998, 2000; Pollitz, 2002; Çakir, 2006; Chaillat et al., 2008, 2009) favor the FMM in their computations as the FMM is well known to provide great reduction in requirement for computational resources (that is CPU and RAM (Random Access Memory)) from incompetent $O(N^2)$ to practical $O(N \log N)$ where N stands for the number of data points. In addition, the FMM provides effective tools to serve as preconditioners suitable for iterative solvers such as GMRES (Generalized Minimum Residual Method; Saad, 2003) (Çakir, 2008; Chaillat et al., 2008, 2009). We utilize the multilevel fast multipole method (MLFMM), which is technically explained in great detail elsewhere (Fujiwara, 1998; Nishimura, 2002; Gumerov et al., 2003). The current method is fast and memory efficient to compute surface wave scattering in local structures due to teleseismic surface wave arrivals where 2.5-D approach is applicable. And also only the perturbing structures need to be discretized, which greatly increases the flexibility of the method.

THEORETICAL FORMULATIONS

Lippman-Schwinger integral equation in 3-D

The fundamental equations of linear elasticity are extensively defined elsewhere (Aki and Richards, 1980) and therefore we omit the respective definitions to start

directly with the Lippman-Schwinger integral equation representation of the 3-D displacement wavefield in the frequency domain (Huang and Fehler, 2000; Bostock et al., 2001; Snieder, 2002), that is in indicial form

$$u_i(\mathbf{x}) = u_i^{(0)}(\mathbf{x}) - \int \left[\frac{\partial}{\partial x'_k} G_{in}^{(0)}(\mathbf{x},\mathbf{x}') \right] c_{nklj}^{(1)}(\mathbf{x}') \frac{\partial}{\partial x'_l} u_j(\mathbf{x}') d\mathbf{x}'$$

(1)

where summations over repeated indices are assumed. The Fredholm integral equation of second kind in (1) utilizes the perturbation theory correct to first order along with the elasticity tensor $\mathbf{c}(\mathbf{x}) = \mathbf{c}^{(0)}(z) + \mathbf{c}^{(1)}(\mathbf{x})$ defined in the Cartesian space $\mathbf{x} = (x, y, z)$ where $\mathbf{c}^{(0)}(z)$ defines the homogeneous (embedding, low frequency) medium and the perturbing volumetric heterogeneities (embedded, high frequency) are given by $\mathbf{c}^{(1)}(\mathbf{x})$. The Green's function (or impulse response) of the homogeneous medium describing the motion excitation at $\mathbf{x}$ (that is evaluation point) in direction i due to a point source at $\mathbf{x}'$ (that is source point) in direction n is given by $G_{in}^{(0)}(\mathbf{x},\mathbf{x}')$. To the incident waves given by $u_i^{(0)}(\mathbf{x})$ are added to these scattered waves off the heterogeneities given by the second term under the integral sign in (1), which we define as $u_i^{(s)}(\mathbf{x})$, that is,

$u_i(\mathbf{x}) = u_i^{(0)}(\mathbf{x}) + u_i^{(s)}(\mathbf{x})$.

In practice, we are unable to solve the equation in (1) analytically since the elastic perturbations have 3-D arbitrary shapes forcing us to resort to numerical resources such as adapted herein. We discretize the arbitrarily shaped volume occupied by $\mathbf{c}^{(1)}(\mathbf{x})$ and then compute contributions of individual pieces each with a simple shape (e.g. a cube). The discretization is performed using sufficiently large number of data points per wavelength (PPW) where PPW values in the range of 3 to 6 usually suffices (Lu et al., 2008). Upon discretization, within each volume defined by $\Delta x \Delta y \Delta z$, the model parameters are assumed constant where $\Delta x = \Delta y = \Delta z = c_{min}/(f_{max}\text{PPW})$ km, which is desampled in accordance with a lower frequency (that is $f < f_{max}$) in the spectrum. The surface wave phase velocity defined by c_{min} corresponds to the slowest surface waves with shortest wavelengths propagating in the medium.

Along the contact between the reference medium (that is $\mathbf{c}^{(0)}$) and heterogeneities (that is $\mathbf{c}^{(1)}$) there exist impedance contrasts causing contact forces and interface forces due to likely displacements of internal layer

boundaries of the reference medium. These two force terms are cancelled by applying Gauss's theorem and partial integration (Maupin, 2001; Snieder, 2002). The wavefield representation in Equation (1) is valid for evaluation points both inside (that is $|\mathbf{x} - \mathbf{x}'| \leq s$) and outside (that is $|\mathbf{x} - \mathbf{x}'| > s$) the heterogeneities with physical size parameterized by s. The densities (ρ) in the medium can also be perturbed, but the influence of density perturbation to the surface wave propagation is only secondary and therefore the representation in (1) includes only the elasticity perturbation. Usually an empirical relation such as $\rho = 0.32\alpha + 0.77$ (Berteussen, 1977), where α is the compressional-wave (or *P*) velocity computed from the shear-wave (or *S*) velocity (β) using Poisson's ratio, is used to obtain the densities (Xia et al., 1999). In addition, we assume that the reference medium and the heterogeneities are isotropic, that is $c_{ijkl} = \lambda \delta_{ij} \delta_{kl} + \mu(\delta_{ik}\delta_{jl} + \delta_{il}\delta_{jk})$ where λ and μ are the Lamé elastic constants and δ_{ij} is the Kronecker delta function (Aki and Richards, 1980).

Let us write the scattered energy in (1) in an expanded form as follows.

$$
\begin{aligned}
u_i^{(s)}(\mathbf{x}) = -\int\Big[&\partial_{x'}G_{ix}^{(0)}(\mathbf{x},\mathbf{x}')\left\{(\lambda^{(1)}+2\mu^{(1)})\partial_{x'}u_x + \lambda^{(1)}(\partial_{y'}u_y + \partial_{z'}u_z)\right\} + \\
&\partial_{y'}G_{iy}^{(0)}(\mathbf{x},\mathbf{x}')\left\{(\lambda^{(1)}+2\mu^{(1)})\partial_{y'}u_y + \lambda^{(1)}(\partial_{x'}u_x + \partial_{z'}u_z)\right\} + \\
&\partial_{z'}G_{iz}^{(0)}(\mathbf{x},\mathbf{x}')\left\{(\lambda^{(1)}+2\mu^{(1)})\partial_{z'}u_z + \lambda^{(1)}(\partial_{x'}u_x + \partial_{y'}u_y)\right\} + \\
&\partial_{y'}G_{ix}^{(0)}(\mathbf{x},\mathbf{x}')\left\{\mu^{(1)}(\partial_{y'}u_x + \partial_{x'}u_y)\right\} + \partial_{z'}G_{ix}^{(0)}(\mathbf{x},\mathbf{x}')\left\{\mu^{(1)}(\partial_{z'}u_x + \partial_{x'}u_z)\right\} + \\
&\partial_{x'}G_{iy}^{(0)}(\mathbf{x},\mathbf{x}')\left\{\mu^{(1)}(\partial_{y'}u_x + \partial_{x'}u_y)\right\} + \partial_{z'}G_{iy}^{(0)}(\mathbf{x},\mathbf{x}')\left\{\mu^{(1)}(\partial_{z'}u_y + \partial_{y'}u_z)\right\} + \\
&\partial_{x'}G_{iz}^{(0)}(\mathbf{x},\mathbf{x}')\left\{\mu^{(1)}(\partial_{z'}u_x + \partial_{x'}u_z)\right\} + \partial_{y'}G_{iz}^{(0)}(\mathbf{x},\mathbf{x}')\left\{\mu^{(1)}(\partial_{z'}u_y + \partial_{y'}u_z)\right\}\Big]d\mathbf{x}'
\end{aligned}
$$

(2)

where the partial derivative over a space coordinate (e.g. $\partial/\partial y$) is denoted by ∂_y and $d\mathbf{x}' = dx'dy'dz'$ stands for volume integration over the heterogeneous area. The expression in (2) is made of several differential potentials summed to give the total scattered wavefield. The following expression can be used to represent any one of these potentials in (2), that is

$$P = -\int \left[\partial_{\xi'} G_{pq}^{(0)}(\mathbf{x},\mathbf{x}') \sigma^{(1)} \partial_{\eta'} u_{\zeta} \right] d\mathbf{x}'$$

(3)

where several supplementary indices (ξ', η', ζ, p, q) are used to represent combinations of space coordinates (x, x', y, y', z, z'). The supplementary parameter $\sigma^{(1)}$ stands for one of the Lamé parameters, that is $\lambda^{(1)}$, $\mu^{(1)}$ or $(\lambda^{(1)} + 2\mu^{(1)})$ representing the model parameter perturbations. In the following, we progressively modify

the representative expression in (3) to attain the proper expression for the 2.5-D displacement.

Rayleigh and Love Green's functions in 3-D

The Rayleigh (R) and Love (L) surface wave Green's functions used in (2) have the following 3-D tensor expressions (Takeuchi and Saito, 1972; Maupin, 2001).

$$^{R}G_{in}^{(0)}(\mathbf{x},\mathbf{x}') = \sum_{k} \begin{pmatrix} -k^{-1}y_3^R(z)\partial_x \\ -k^{-1}y_3^R(z)\partial_y \\ -y_1^R(z) \end{pmatrix} \left(-k^{-1}y_3^R(z')\partial_{x'} \quad -k^{-1}y_3^R(z')\partial_{y'} \quad -y_1^R(z') \right) \frac{-j}{8ucI_1}H_0^{(2)}(kr)$$

(4a)

$$^{L}G_{in}^{(0)}(\mathbf{x},\mathbf{x}') = \sum_{k} \begin{pmatrix} k^{-1}y_1^L(z)\partial_y \\ -k^{-1}y_1^L(z)\partial_x \\ 0 \end{pmatrix} \left(k^{-1}y_1^L(z')\partial_{y'} \quad -k^{-1}y_1^L(z')\partial_{x'} \quad 0 \right) \frac{-j}{8ucI_1}H_0^{(2)}(kr)$$

(4b)

where $k^2 = k_x^2 + k_y^2$ and $r^2 = (x-x')^2 + (y-y')^2$. The Rayleigh waves made of compressional (P) and vertically polarized shear waves (SV) are excited by the three components (that is F_x, F_y and F_z) of a single-force $\mathbf{F}$ whilst the Love waves made of horizontally polarized shear waves (SH) are excited by only horizontal force components (that is F_x and F_y). Herein y_1^R (vertical) and y_3^R (horizontal) represent Rayleigh surface wave displacement eigenfunctions as a function of depth. Similarly y_1^L a function of depth represents the displacement eigenfunction of Love surface wave modes. The surface wave motion generally includes fundamental and higher modes propagating independently from each other. The total wavefield is made of linear combination of these modes as the sum over modes represented by k (horizontal wavenumber) implies. In Equations (4a) and (4b), the parameters c, u and I_1 explain the modal phase velocity, group velocity and energy integral, respectively whilst $j = \sqrt{-1}$. The complex exponential $e^{j\omega t}$, which is used to attain the temporal (t – time) amplitudes via an inverse Fourier transform (ω – angular frequency), is suppressed in the Green's function expressions above.

In order to compute the dispersion parameters of the embedding structure in Equations (4a) and (4b), we use a stable normal mode algorithm (Abo-Zena, 1979; Chen, 1993) considering a layered Cartesian structure over a half-space. The propagating medium is assumed to intrinsically attenuate the wavefield over the horizontal distance (r), that is, the surface wave amplitudes are multiplied by $e^{-\omega r/2Qu}$ where the modal quality factor Q is determined via the variational principle (Aki and Richards, 1980) along with complex layer velocities defined through

P- and S-wave quality factors in the embedding. The Hankel function of second kind and zeroth order [that is $H_0^{(2)}(kr)$] in the Green's functions, as standing for only outward propagating surface waves, defines the geometrical spreading including both near- and far-field effects on the amplitude and phase.

In performing the scattering computations in Equation (2), we consider phase conversions of Rayleigh-to-Love and Love-to-Rayleigh as well as Rayleigh-to-Rayleigh and Love-to-Love off the heterogeneities. When the higher mode surface wave propagation is considered, the mode coupling between various Rayleigh and Love modes is also taken into account. In certain cases, the heterogeneities may also convert some part of surface wave energy to body waves for which case we create a quasi-waveguide adding extra fast, sufficiently deep cap layer below the crust (e.g. at 300-km depth). Such extended structure allows more surface wave modes to exist in the propagating medium, which consequently allows better representation of steeply traveling body waves (Maupin, 2001).

The computation of synthetic seismograms using the normal mode theory (NMT) involves a general three-stage mechanism. The first stage involves computations of displacement eigenfunction at depth corresponding to the source point. In the second stage, the source term is propagated to the evaluation point in the horizontal plane. And, in the third stage, the displacement eigenfunction computed at depth corresponding to the evaluation point is used to obtain the final amplitude. In the present work, we employ the MLFMM in the second stage to accelerate the expensive computation of interactions between the source and evaluation points eigenfunction.

Figure 2 shows that the anomalous volume (or velocity perturbation) at depth is discretized at certain rate. The source contributions denoted by $A(x',y',z')$ due to the anomalous structure are properly weighted by the corresponding surface wave eigenfunctions at depth and then these amplitudes are vertically integrated using the trapezoidal rule that results the amplitude distribution $B(x',y')$ in the horizontal plane (left panel in Figure 2). As shown in the middle panel, through various levels upward and downward passes the MLFMM integrates the latter amplitudes over the horizontal plane to result another amplitude distribution denoted by $C(x,y)$. In the final step, the $C(x,y)$ amplitudes are weighted by the evaluation point eigenfunctions at depth to result the amplitudes $D(x,y,z)$, which are used to compute the wavefield at a target point (right panel in Figure 2).

Modification of integral equation

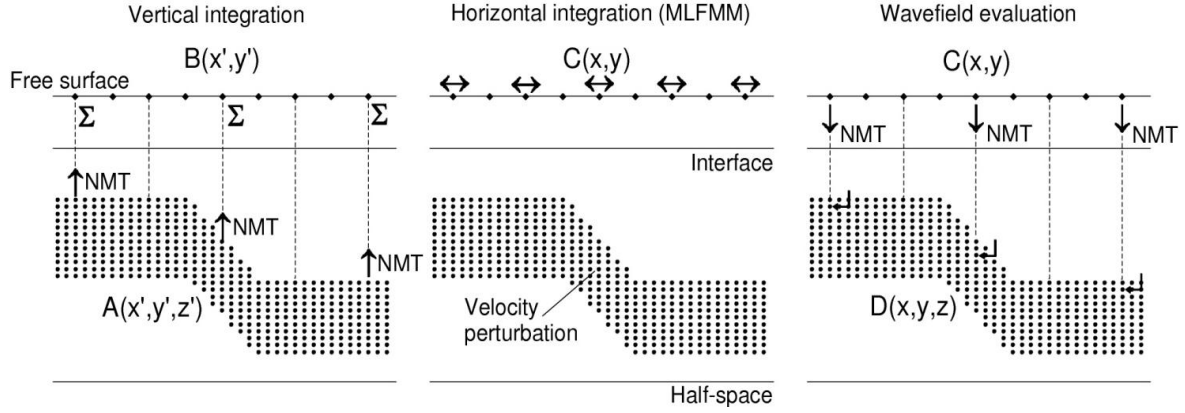The integral in Equation (3) can also be written as follows:

Figure 2. The normal mode theory (NMT) and the multilevel fast multipole method (MLFMM) are combined as shown in the schema. The anomalous volume at depth is shown discretized.

$$P = -\int \left[\partial_{\xi'} \left\{ \overline{G}_{pq}^{(0)}(\mathbf{x}, \mathbf{x}') H_0^{(2)}(kr) \right\} \sigma^{(1)} \partial_{\eta'} u_{\zeta} \right] d\mathbf{x}' \qquad (5)$$

where we basically factor out the Hankel function in Equations (4a) and (4b) to define a slightly different Green's function given by $\overline{G}_{pq}^{(0)}(\mathbf{x}, \mathbf{x}')$, that is:

$$^{R,L}\overline{G}_{in}^{(0)}(\mathbf{x}, \mathbf{x}') = \frac{1}{H_0^{(2)}(kr)} {}^{R,L}G_{in}^{(0)}(\mathbf{x}, \mathbf{x}') \qquad (6)$$

We continue modifying the expression in Equation (3) by substituting the below (plane-wave decomposition) integral for the Hankel function (Wenzel et al., 1990)

$$H_0^{(2)}(kr) = \pi^{-1} \int_{-\infty}^{\infty} k_x^{-1} e^{-j\left[k_y(y-y') + k_x|x-x'|\right]} dk_y \qquad (7)$$

It follows that

$$P = -\int \left[\partial_{\xi'} \left\{ \overline{G}_{pq}^{(0)}(\mathbf{x}, \mathbf{x}') \pi^{-1} \int_{-\infty}^{\infty} k_x^{-1} e^{-j\left[k_y(y-y') + k_x|x-x'|\right]} dk_y \right\} \sigma^{(1)} \partial_{\eta'} u_{\zeta} \right] d\mathbf{x}' \qquad (8)$$

Let us now assume that the local (or regional) structure has only two-dimensional (2-D) variations as shown in Figure 1. The general strike of regional geology is in the y-direction whereas the direction of geological change is in the x-direction, that is $\lambda^{(1)} = \lambda^{(1)}(x', z')$ and $\mu^{(1)} = \mu^{(1)}(x', z')$. The surface waves can arrive from an arbitrary backazimuth creating scattering also in the y-direction. Therefore, the displacements are essentially 3-D even though the underground geology has only 2-D features. We assume that the surface waves have

teleseismic arrival with planar (or quasi-planar) wavefront represented by a certain horizontal wave number $\tilde{\mathbf{k}} = \mathbf{e}_x \tilde{k}_x + \mathbf{e}_y \tilde{k}_y$. If the backazimuth (BAZ) and the horizontal slowness ($\tilde{s}$) are used, then $\tilde{k}_x = -\omega \tilde{s} \cos(\text{BAZ})$ and $\tilde{k}_y = -\omega \tilde{s} \sin(\text{BAZ})$.

Albeit the displacements are 3-D, the waves in the y-direction still scatter independent of overall scattering of waves in the vertical (or sagittal) plane as predicted by Snell's law (Papageorgiou and Pei, 1998; Bostock et al., 2001; Bostock, 2002). In this respect, the following relation holds (Papageorgiou and Pei, 1998).

$$u_i(x', y', z') = \tilde{c}_y^{-1} \hat{u}_i(x', \tilde{k}_y, z') e^{-j\tilde{k}_y y'} \qquad (9)$$

where $\hat{\mathbf{u}}$ stands for the Fourier transform of the wavefield with respect to y' and $\tilde{c}_y$ represents the y-component of the horizontal phase velocity of the incident waves. If we evaluate the expression in (9) at another arbitrary location (that is at $y' = \tilde{y}'$), then we get

$$\tilde{u}_i(x', y' = \tilde{y}', z') = \tilde{c}_y^{-1} \hat{u}_i(x', \tilde{k}_y, z') e^{-j\tilde{k}_y \tilde{y}'} \qquad (10)$$

From the ratio of expressions in Equations (9) and (10), we get the following expression that connects the wavefields at these two locations (y' and $\tilde{y}'$) taking place along the geological strike (or y-axis).

$$u_i(x', y', z') = \tilde{u}_i(x', y' = \tilde{y}', z') e^{-j\tilde{k}_y(y' - \tilde{y}')} \qquad (11)$$

Substituting the expression (11) in (8) yields:

$$P = -\int \left[\partial_{\xi'} \left\{ \overline{G}_{pq}^{(0)}(\mathbf{x}, \mathbf{x}') \pi^{-1} \int_{-\infty}^{\infty} k_x^{-1} e^{-j\left[k_y(y-y') + k_x|x-x'|\right]} dk_y \right\} \sigma^{(1)} \partial_{\eta'} \left\{ \tilde{u}_{\zeta} e^{-j\tilde{k}_y(y' - \tilde{y}')} \right\} \right] d\mathbf{x}'$$

$$\qquad (12)$$

Depending on the particular tensor component of the Rayleigh or Love surface waves, the integrand in (12) includes various spatial differentiations at both evaluation and source points [Equations (4a) and (4b)]. A close inspection of Equation (12) shows that in each case of different tensor component, we can isolate these terms dependent solely on the independent variable y' after explicitly performing the corresponding spatial differentiations. Therefore, Equation (12) can be put in the following abstract form.

$$P = -\int \left[\left\{ \pi^{-1} \int_{-\infty}^{\infty} k_x^{-1} \kappa_1 e^{-j[k_y(y-y')+k_x|x-x'|]} dk_y \right\} \left\{ \sigma^{(1)} \kappa_2 e^{-j\tilde{k}_y(y'-\tilde{y}')} \partial_\eta \bar{u}_\zeta \right\} \right] d\mathbf{x}'$$

(13)

where we have introduced two new variables as κ_1 and κ_2. These two variables can be a function of different parameters combined (e.g. k_x, k_y, $\tilde{k}_y$ or unity), but not a function of y'. Then the integration on y' is isolated by changing the integration order whilst gathering the y' dependent terms together as follows.

$$P = -\iint \left[\pi^{-1} \int_{-\infty}^{\infty} \left\{ k_x^{-1} \kappa_1 e^{-jk_x|x-x'|} e^{-j(k_y-\tilde{k}_y)\tilde{y}'} \left(\int_{-\infty}^{\infty} e^{j(k_y-\tilde{k}_y)y'} dy' \right) \right\} dk_y \sigma^{(1)} \kappa_2 \partial_\eta \bar{u}_\zeta \right] dx' dz'$$

(14)

which after Fourier transform with respect to y', yields

$$P = -2\iint \left[\int_{-\infty}^{\infty} \left\{ k_x^{-1} \kappa_1 e^{-jk_x|x-x'|} e^{-j(k_y y-\tilde{k}_y \tilde{y}')} \delta(k_y - \tilde{k}_y) \right\} dk_y \sigma^{(1)} \kappa_2 \partial_\eta \bar{u}_\zeta \right] dx' dz'$$

(15a)

Using the properties of the Dirac delta function, we can further simplify the expression in (14), that is

$$P = -2\iint \left[k_x^{-1} \kappa_1 e^{-jk_x|x-x'|} e^{-j\tilde{k}_y(y-\tilde{y}')} \sigma^{(1)} \kappa_2 \partial_\eta \bar{u}_\zeta \right] dx' dz'$$

(15b)

We can now reverse the effect of temporary variables κ_1 and κ_2 to write that

$$P = -\iint \left[\partial_{\xi'} \tilde{G}_{pq}^{(0)}(\mathbf{x}, x', z'; \tilde{y}') \sigma^{(1)}(x', z') \partial_\eta \tilde{u}_\zeta(x', z'; \tilde{y}') \right] dx' dz' \quad (16)$$

Rayleigh and Love Green's functions in 2.5-D

The modified Rayleigh (R) and Love (L) Green's functions that can be used in the 2.5-D surface wave scattering computations have the following definitions.

$$^R\tilde{G}_{in}^{(0)}(\mathbf{x}, x', z'; \tilde{y}') = \sum_k \begin{pmatrix} -k^{-1} y_3^R(z)\partial_x \\ k^{-1} y_3^R(z)j\tilde{k}_y \\ -y_1^R(z) \end{pmatrix} \begin{pmatrix} -k^{-1} y_3^R(z')\partial_{x'} & -k^{-1} y_3^R(z')j\tilde{k}_y & -y_1^R(z') \end{pmatrix} \frac{-j}{4ucI_1} \Omega$$

(17a)

$$^L\tilde{G}_{in}^{(0)}(\mathbf{x}, x', z'; \tilde{y}') = \sum_k \begin{pmatrix} -k^{-1} y_1^L(z)j\tilde{k}_y \\ -k^{-1} y_1^L(z)\partial_x \\ 0 \end{pmatrix} \begin{pmatrix} k^{-1} y_1^L(z')j\tilde{k}_y & -k^{-1} y_1^L(z')\partial_{x'} & 0 \end{pmatrix} \frac{-j}{4ucI_1} \Omega$$

(17b)

where

$$\Omega = k_x^{-1} e^{-j[\tilde{k}_y(y-\tilde{y}')+k_x|x-x'|]}$$

(17c)

$$k_x = \begin{cases} \sqrt{k^2 - \tilde{k}_y^2}, & k \geq \tilde{k}_y \\ -j\sqrt{\tilde{k}_y^2 - k^2}, & k < \tilde{k}_y \end{cases}$$

(17d)

There are two special cases in Equation (16) regarding the differentiation with respect to y' that we have used to define the Green's functions in Equations (17a) to (17d), that is $\partial_{\eta'}\tilde{u}_\zeta \equiv -j\tilde{k}_y \tilde{u}_\zeta$ if $\partial_{\eta'} \equiv \partial_{y'}$ and also $\partial_{\xi'}\tilde{G}_{pq}^{(0)} \equiv j\tilde{k}_y \tilde{G}_{pq}^{(0)}$ if $\partial_{\xi'} \equiv \partial_{y'}$.

Lippman-Schwinger integral equation in 2.5-D

Considering the assumptions made earlier, the 3-D Lippman-Schwinger integral equation in (1) takes the following form.

$$u_i(\mathbf{x}) = u_i^{(0)}(\mathbf{x}) - \int_{-\infty}^{\infty} dx' \int_0^{\infty} \partial_{k'} \tilde{G}_{in}^{(0)}(\mathbf{x}, x', z'; \tilde{y}') c_{nklj}^{(1)}(x', z') \partial_l \tilde{u}_j(x', z'; \tilde{y}') dz'$$

(18)

where the perturbed wavefield is effectively solved in the vertical plane (x', z') corresponding to $y' = \tilde{y}'$. Here $\tilde{y}'$ can also be set to zero without changing the generality of the algorithm.
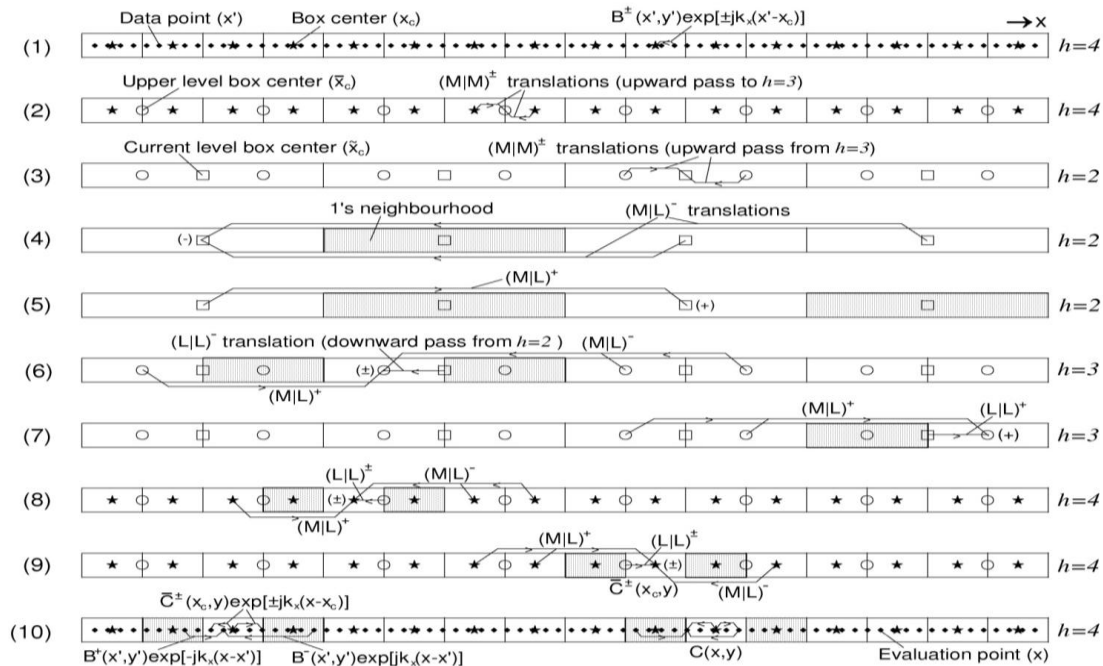
Figure 3. The multilevel fast multipole method is illustrated using various levels translation operators on a tree structure. The plus and minus signs indicate all outward motions. The arrows are used to indicate the direction of translations where consolidations take place.

Application of MLFMM

We build our MLFMM application on top of these complex exponentials in the 2.5-D Green's functions in Equations (17a)-(17d) that define the wave propagation in the horizontal plane. Note that the distance between the source and evaluation points is measured as absolute along the *x*-direction. Therefore, we construct our MLFMM algorithm in two parts separating the waves as traveling outward in the positive and negative directions. It follows that if $x > x'$ (positive direction),

$$\left[e^{-jk_x(x-x')}\right]e^{-j\tilde{k}_y(y-\tilde{y}')} = \left[e^{-jk_x(x-x_c)}e^{jk_x(x'-x_c)}\right]e^{-j\tilde{k}_y(y-\tilde{y}')} \quad (19a)$$

where the complex exponential in (17c) is interpreted in terms of an expansion centre at x_c. Similarly, for another expansion centre at $\bar{x}_c$

$$\left[e^{-jk_x(x-x')}\right]e^{-j\tilde{k}_y(y-\tilde{y}')} = \left[e^{-jk_x(x-\bar{x}_c)}e^{jk_x(x'-\bar{x}_c)}\right]e^{-j\tilde{k}_y(y-\tilde{y}')} \quad (19b)$$

The two expansions in (19a) and (19b) can be connected via the multipole-to-multipole $[(M \mid M)^+]$ translation operator given as follows.

$$(M \mid M)^+ = e^{-jk_x(\bar{x}_c-x_c)} \quad (19c)$$

Moreover, if $x < x'$ (negative direction), the two expansions with respect to x_c and $\tilde{x}_c$ can have the following expressions.

$$\left[e^{jk_x(x-x')}\right]e^{-j\tilde{k}_y(y-\tilde{y}')} = \left[e^{jk_x(x-x_c)}e^{-jk_x(x'-x_c)}\right]e^{-j\tilde{k}_y(y-\tilde{y}')} \quad (19d)$$

$$\left[e^{jk_x(x-x')}\right]e^{-j\tilde{k}_y(y-\tilde{y}')} = \left[e^{jk_x(x-\bar{x}_c)}e^{-jk_x(x'-\bar{x}_c)}\right]e^{-j\tilde{k}_y(y-\tilde{y}')} \quad (19e)$$

And the corresponding multipole-to-multipole $[(M \mid M)^-]$ translation operator takes the form

$$(M \mid M)^- = e^{jk_x(\bar{x}_c-x_c)} \quad (19f)$$

The other two translation operators, that is, multipole-to-local $[(M \mid L)^\pm]$ and local-to-local $[(L \mid L)^\pm]$, have the same functional forms as $[(M \mid M)^\pm]$ in Equations (19c) and (19f), respectively.

Figure 3 illustrates the MLFMM scheme on a 1-D data structure where the maximum tree level ($h_{\max}$) is set to four. The first active level is $h = 2$. The data structure includes 16 boxes corresponding to $2^{h_{\max}}$ and each box is represented by a box centre (x_c) used as expansion centre. A binary-tree space subdivision represents the 1-D data hierarchy and the slight thickness in the

y-direction is used for only demonstration where $y = y' = \widetilde{y}'$ is implemented. As shown in the topmost panel, we create expansion coefficients $B^{\pm}$ for each data point at x' with respect to the box centre x_c to which the data point belongs and then these expansion coefficients are consolidated to obtain one expansion coefficient per box centre. Note that two expansion coefficients (that is B^+ and B^-) per data point are prepared to account for the waves traveling outward in both positive and negative directions.

The higher level coefficients consolidated at $h = 4$ are

$(M \mid M)^{\pm}$ translated (that is upward pass) and are consolidated at a lower level (that is $h = 3$) as one instance shows in the second panel from top. As shown in the third panel, the upward pass and consolidation processes are similarly repeated for another lower tree level, which continues until the minimum tree level (that is $h_{\min} = 2$) at which level the downward passes start. The fourth and fifth panels show the $(M \mid L)^-$ and $(M \mid L)^+$ translations from the distance range outside the 1's neighborhood (shaded area) in the minimum tree level applied to waves traveling in the negative direction

$$^\gamma D u_i^{(s)}(\mathbf{x}) = e^{-j\widetilde{k}_y(y-\widetilde{y}')}\left[D_x^\gamma e^{-jk_x(x-x_c)} \int_{-\infty}^{\infty} D_{x'}^\gamma e^{jk_x(x'-x_c)} dx' + D_x^\gamma e^{jk_x(x-x_c)} \int_{-\infty}^{\infty} D_{x'}^\gamma e^{-jk_x(x'-x_c)} dx' \right] \tag{20}$$

(forth panel) and in the positive direction (fifth panel), respectively. The latter coefficients are then $(L \mid L)^-$ or $(L \mid L)^+$ translated (that is downward pass) depending on the particular wave propagation direction and are added to the $(M \mid L)^{\pm}$ translated coefficients at higher level tree (that is $h = 3$) as one instance shows in the sixth panel. The seventh panel shows another instance of downward pass at $h = 3$ where only waves traveling in the positive direction are valid. The eighth and ninth panels show various instances of downward passes at $h = 4$ in the positive and negative directions. The resulting coefficients defined by $\overline{C}^{\pm}(x_c, y)$ are temporarily stored to use them to obtain the final MLFMM coefficients given by $C(x, y)$ shown in the bottom panel. Note that some near-field coefficients not treated within the MLFMM are added to the MLFMM coefficients as one instance shows in the lower left of Figure 3.

After inserting the multipole expansions in (19a) and (19d) into the integral equation in (18), factoring out the common terms and rearranging, one can rewrite the scattering part of the integral equation in (18) as a collection of dot products, that is the partial derivative operators, that is, D_x^γ and $D_{x'}^\gamma$, correspond to spatial differentiations at evaluation and source locations, respectively. The derivative operator $D_{x'}^R$ corresponding to the Rayleigh surface waves has the following definition.

$$D_{x'}^R(x') = \frac{jk_x^{-1}}{4ucI_1} k^{-1}\left(k^{-1}\left[R_1\partial_{x'}^2 - R_2\widetilde{k}_y^2 + 2R_4 j\widetilde{k}_y\partial_{x'} + R_5\partial_{x'} + R_6 j\widetilde{k}_y\right] + R_3 + R_7\partial_{x'} + R_8 j\widetilde{k}_y\right) \tag{21}$$

where the first integral is for the waves traveling outward in the positive direction and the second integral, for the waves traveling outward in the negative direction. The algorithm in Equation (20) is performed multiple times for each surface wave mode traveling independently from each other in the medium. Here, $\gamma = R$ represents a Rayleigh surface wave mode and $\gamma = L$ stands for a Love surface wave mode.

The partial derivative operators, that is D_x^γ and $D_{x'}^\gamma$, correspond to spatial differentiations at evaluation and source locations, respectively. The derivative operator $D_{x'}^R$ corresponding to the Rayleigh surface waves has the following definition.

In Equation (21), the wave potentials R_i $(i = 1, 2, \ldots, 8)$ functions of displacement and displacement gradients and also of heterogeneities of the medium have the following expressions.

$$R_1(x') = \int \left(\chi(x', z')\partial_{x'}u_x(x', z') + \lambda^{(1)}(x', z')\left[j\widetilde{k}_y u_y(x', z') + \partial_{z'}u_z(x', z')\right]\right) y_3^R(z') dz' \tag{22a}$$

$$R_2(x') = \int \left(\chi(x', z')j\widetilde{k}_y u_y(x', z') + \lambda^{(1)}(x', z')\left[\partial_{x'}u_x(x', z') + \partial_{z'}u_z(x', z')\right]\right) y_3^R(z') dz' \tag{22b}$$

$$R_3(x') = \int \left(\chi(x', z')\partial_{z'}u_z(x', z') + \lambda^{(1)}(x', z')\left[\partial_{x'}u_x(x', z') + j\widetilde{k}_y u_y(x', z')\right]\right) \partial_{z'} y_1^R(z') dz' \tag{22c}$$

$$R_4(x') = \int \left(\mu^{(1)}(x', z')\left[j\widetilde{k}_y u_x(x', z') + \partial_{x'}u_y(x', z')\right]\right) y_3^R(z') dz' \tag{22d}$$

$$R_5(x') = \int \left(\mu^{(1)}(x', z')\left[\partial_{z'}u_x(x', z') + \partial_{x'}u_z(x', z')\right]\right) \partial_{z'} y_3^R(z') dz' \tag{22e}$$

$$R_6(x') = \int \left(\mu^{(1)}(x', z')\left[\partial_{z'}u_y(x', z') + j\widetilde{k}_y u_z(x', z')\right]\right) \partial_{z'} y_3^R(z') dz' \tag{22f}$$

$$R_7(x') = \int \left(\mu^{(1)}(x', z')\left[\partial_{z'}u_x(x', z') + \partial_{x'}u_z(x', z')\right]\right) y_1^R(z') dz' \tag{22g}$$

$$R_8(x') = \int \left(\mu^{(1)}(x', z')\left[\partial_{z'}u_y(x', z') + \partial_{y'}u_z(x', z')\right]\right) y_1^R(z') dz' \tag{22h}$$

Table 1. List of parameters to build the partial derivative operator D_x^R of the impinging Rayleigh surface waves at the evaluation points.

Parameter	u_x	u_y	u_z
1	$y_3^R(z)\partial_x$	$-y_3^R(z)\mathrm{j}\tilde{k}_y$	$y_1^R(z)$
∂_x	$y_3^R(z)\partial_x^2$	$-y_3^R(z)\mathrm{j}\tilde{k}_y\partial_x$	$y_1^R(z)\partial_x$
∂_y	$-y_3^R(z)\mathrm{j}\tilde{k}_y\partial_x$	$-y_3^R(z)\tilde{k}_y^2$	$-y_1^R(z)\mathrm{j}\tilde{k}_y$
∂_z	$\partial_z y_3^R(z)\partial_x$	$-\partial_z y_3^R(z)\mathrm{j}\tilde{k}_y$	$\partial_z y_1^R(z)$

Table 2. List of parameters to build the partial derivative operator D_x^L of the impinging Love surface waves at the evaluation points.

Parameter	u_x	u_y	u_z
1	$-y_1^L(z)\mathrm{j}\tilde{k}_y$	$-y_1^L(z)\partial_x$	0
∂_x	$-y_1^L(z)\mathrm{j}\tilde{k}_y\partial_x$	$-y_1^L(z)\partial_x^2$	0
∂_y	$-y_1^L(z)\tilde{k}_y^2$	$y_1^L(z)\mathrm{j}\tilde{k}_y\partial_x$	0
∂_z	$-\partial_z y_1^L(z)\mathrm{j}\tilde{k}_y$	$-\partial_z y_1^L(z)\partial_x$	0

where $\chi(x',z') = \left[\lambda^{(1)}(x',z') + 2\mu^{(1)}(x',z')\right]$. Similarly, the derivative operator $D_{x'}^L$ corresponding to the Love surface waves has the following definition.

$$D_{x'}^L(x') = \frac{\mathrm{j}k_x^{-1}}{4ucI_1}k^{-2}\left[(L_1 - L_2)\mathrm{j}\tilde{k}_y\partial_{x'} - L_3\tilde{k}_y^2 + L_4\mathrm{j}\tilde{k}_y - L_3\partial_{x'}^2 - L_5\partial_{x'}\right]$$

(23)

In Equation (23), the wave potentials L_i ($i = 1,2,\ldots,5$) functions of displacement and displacement gradients and also of heterogeneities of the medium have the following expressions.

$$L_1(x') = \int\left(\chi(x',z')\partial_{x'}u_x(x',z') + \lambda^{(1)}(x',z')\left[\mathrm{j}\tilde{k}_y u_y(x',z') + \partial_z u_z(x',z')\right]\right)y_1^L(z')dz'$$

(24a)

$$L_2(x') = \int\left(\chi(x',z')\mathrm{j}\tilde{k}_y u_y(x',z') + \lambda^{(1)}(x',z')\left[\partial_{x'}u_x(x',z') + \partial_z u_z(x',z')\right]\right)y_1^L(z')dz'$$

(24b)

$$L_3(x') = \int\left(\mu^{(1)}(x',z')\left[\mathrm{j}\tilde{k}_y u_x(x',z') + \partial_{x'}u_y(x',z')\right]\right)y_1^L(z')dz'$$

(24c)

$$L_4(x') = \int\left(\mu^{(1)}(x',z')\left[\partial_{z'}u_x(x',z') + \partial_{x'}u_z(x',z')\right]\right)\partial_{z'}y_1^L(z')dz'$$

(24d)

$$L_5(x') = \int\left(\mu^{(1)}(x',z')\left[\partial_{z'}u_y(x',z') + \mathrm{j}\tilde{k}_y u_z(x',z')\right]\right)\partial_{z'}y_1^L(z')dz'$$

(24e)

The necessary parameters to build the second derivative operator in Equation (20), that is D_x^γ, are listed in Table 1 for the Rayleigh surface waves (D_x^R) and in Table 2 for the Love surface waves (D_x^L). Intersecting rows and columns in Tables 1 and 2 are used to construct the corresponding derivatives. For instance, if the z-gradient of the x-component of displacement (that is $\partial_z u_x$) due to an impinging Rayleigh surface wave mode is considered, then $D_x^R = \partial_z y_3^R(z)\partial_x$, which is found from the intersection of ∂_z (last row) and u_x (second column) in Table 1. The third derivative operator $^\gamma D$ in Equation (20) is used to identify if the outcome of Equation (20) is either displacement or displacement gradient. This
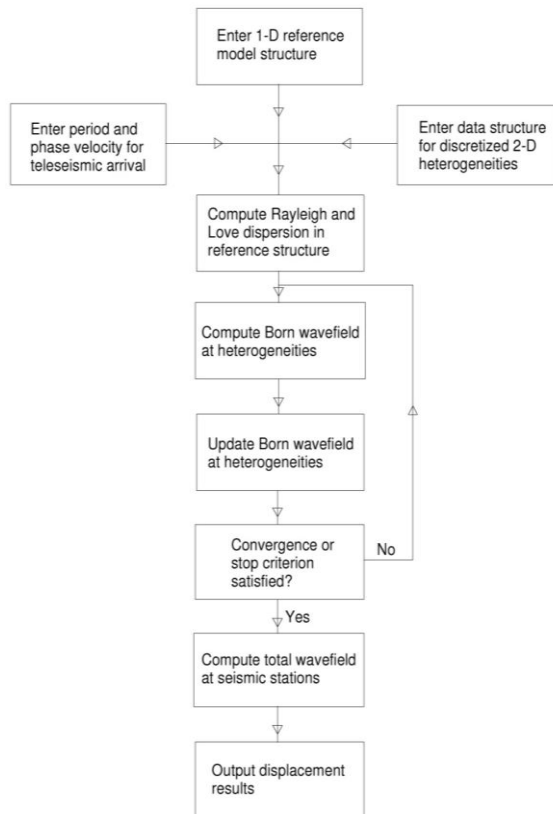
Figure 4. A pseudo-code for the current algorithm is shown.

Figure 5. The 2-D model structure used for the current numerical calculations is shown.

operator ($^\gamma D$) is equal to the corresponding spatial partial (e.g. ∂_x) if the outcome is a displacement gradient. If, on the other hand, the outcome is a displacement, then it is equal to unity.

We symbolically use $\tilde{\mathbf{k}}_i$ to show that the teleseismic surface wave arrival at certain frequency may also include a few higher mode arrivals, in addition to the usual fundamental mode arrival. If such multimode surface wave propagation is considered, one then performs the wavefield computations in (1) as many times as the number of arriving modes and then sum up the individual mode contributions to get the total wavefield. Therefore, the incident waves represented by $u_i^{(0)}(\mathbf{x})$ in (1) change in accordance with the arriving surface wave mode. For instance,

$$u_i(\mathbf{x}) = \left(^{R_{FM}}u_i^{(0)}(\mathbf{x}) + {}^{R_{FM}}u_i^{(s)}(\mathbf{x})\right) + \left(^{R_{FH}}u_i^{(0)}(\mathbf{x}) + {}^{R_{FH}}u_i^{(s)}(\mathbf{x})\right) + \left(^{R_{SH}}u_i^{(0)}(\mathbf{x}) + {}^{R_{SH}}u_i^{(s)}(\mathbf{x})\right)$$
$$+ \left(^{L_{FM}}u_i^{(0)}(\mathbf{x}) + {}^{L_{FM}}u_i^{(s)}(\mathbf{x})\right) + \left(^{L_{FH}}u_i^{(0)}(\mathbf{x}) + {}^{L_{FH}}u_i^{(s)}(\mathbf{x})\right) + \left(^{L_{SH}}u_i^{(0)}(\mathbf{x}) + {}^{L_{SH}}u_i^{(s)}(\mathbf{x})\right)$$
$$(25)$$

where Rayleigh surface wave arrivals of fundamental mode (R_{FM}), first higher mode (R_{FH}) and second

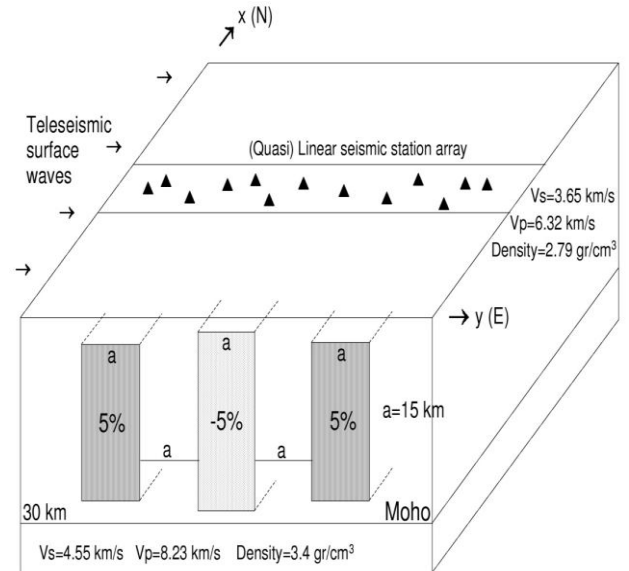higher mode (R_{SH}) are simultaneously considered. Similarly, fundamental (L_{FM}), first higher (L_{FH}) and second higher (L_{SH}) Love surface wave modes are also considered to teleseismically arrive.

Figure 4 gives a pseudo-code to show how the current algorithm runs. A 1-D spherical model structure characterizing the background (or reference) velocity structure is introduced into the source code. Since we carry out our surface wave calculations assuming flat structure, we perform spherical-to-flat transforms (Schwab and Knopoff, 1972) to take the Earth's sphericity into account. The phase velocity and period of the respective teleseismic surface wave (Rayleigh or Love) arrival and also data structure for the discretized 2-D heterogeneities are provided as input into the source code. Both incident and scattered waves travel in the reference structure for which we compute Rayleigh and Love surface wave dispersion considering multimode propagation. The Born approximation (Maupin, 2001) suffices for the current scattering calculations. Therefore we first compute the wavefield at heterogeneities replacing the total wavefield by the incident wavefield and then update the wavefield in the propagating medium. A stopping criterion based on convergence or maximum number of iterations is set to terminate the Born series. Once this criterion is satisfied, the wavefield at the seismic stations are finally computed.

NUMERICAL EXAMPLES

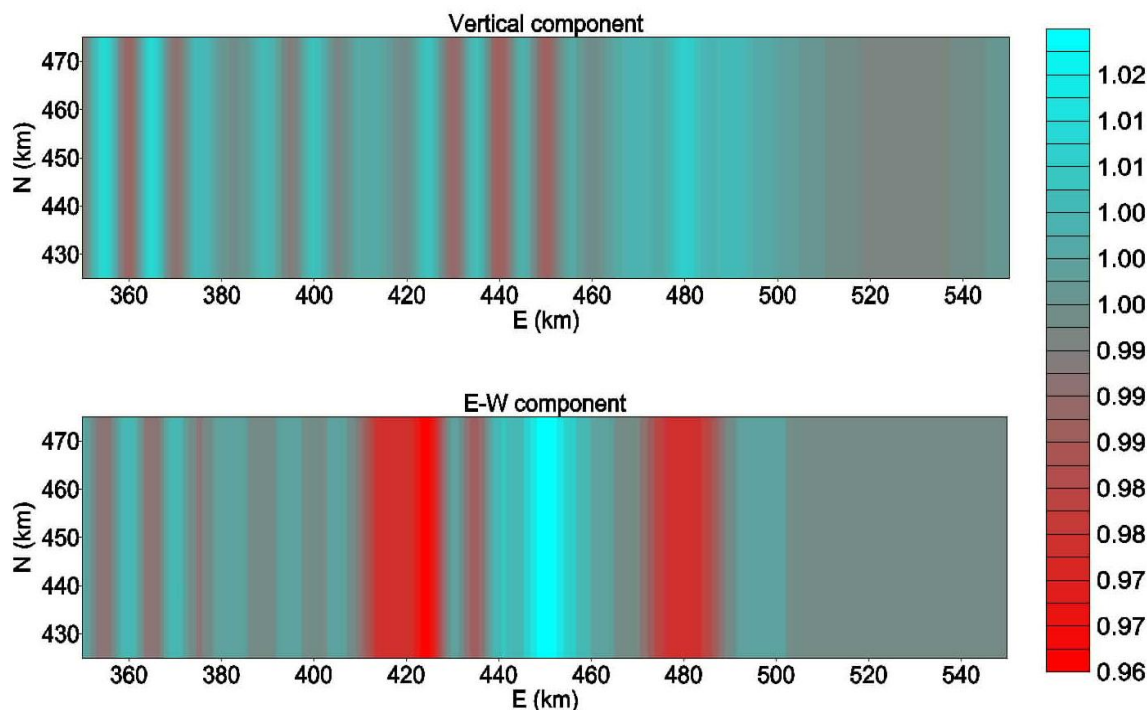The 2-D model structure used to perform numerical experiments is shown in Figure 5 where the reference

Figure 6. Rayleigh surface wave (vertical and E-W or radial component) displacements are shown upon teleseismic fundamental mode Rayleigh surface wave arrival from the west onto the structure given in Figure 5 (Rayleigh surface wave scattering results).

structure is simply made of one-layer crust overlying a half-space. The model parameters are listed in Figure 5. The propagating medium is assumed attenuating characterized by *P*- and *S*-wave quality factors, that is $Q_s = 100$ and $Q_p = 2.25 Q_s$. The crust layer is modestly perturbed by three inclusions each with 5% perturbation. The inclusion with a slightly different depth range in the middle slows the wavefield whilst the two inclusions on either side are faster. The linear (or quasi-linear) seismic station array is spread over the perturbed region approximately perpendicular to the geological strike (that is N-S direction in Figure 5). Planar (or quasi-planar) teleseismic surface waves are assumed to arrive from the west perpendicular to the geological strike, which makes current surface wave scattering calculations effectively 2-D; that is showing no changes with respect to current *x*-axis (North).

We presently assume that teleseismic Rayleigh and Love fundamental modes are emergent from the west with 6.25 s period and 3.34 and 3.68 km/s phase velocities, respectively. At this period the background 1-D velocity structure supports 2 Rayleigh and 2 Love surface wave modes; that is fundamental mode plus one higher mode. We do not include the effect of body waves that scatter at high incidence angles corresponding to phase velocities greater than that of normal modes in the propagating medium (Maupin, 2001). The seismic stations are spread over the region of interest placed at

the surface with 5-km interval in both N-S and E-W directions. The 2-D model structure is discretized using PPW=6. In case of emergent Rayleigh surface waves, we show vertical and E-W (or radial) component displacements computed at the seismic stations whilst N-S (or tangential) component displacements are negligible. And in case of emergent Love surface waves, we show N-S (or tangential) component displacements at the stations whilst vertical and E-W (or radial) component displacements are negligible.

In Figure 6, we first show the scattering results due to the incident fundamental mode Rayleigh surface waves. The upper panel corresponds to the vertical component whilst the lower panel depicts E-W (or radial) component. The spectral amplitudes are shown after normalization with respect to the reference medium amplitudes. The obstacles each with 15-km width have central locations placed at 420, 450 and 480 km along the E-W direction. As seen from the E-W component amplitudes, the horizontal motions are mostly trapped within the obstacles. The anomalous structures act as barriers blocking the passage of horizontally polarized Rayleigh waves resulting mostly back scattering and relatively weaker forward scattering. Compared to the E-W component, the vertically polarized Rayleigh surface waves are less affected from the obstacles, as seen from the vertical component amplitudes. Both back scattering and forward scattering mechanisms are valid, but significant part of the vertically polarized Rayleigh surface wave energy is able to continue pass through the
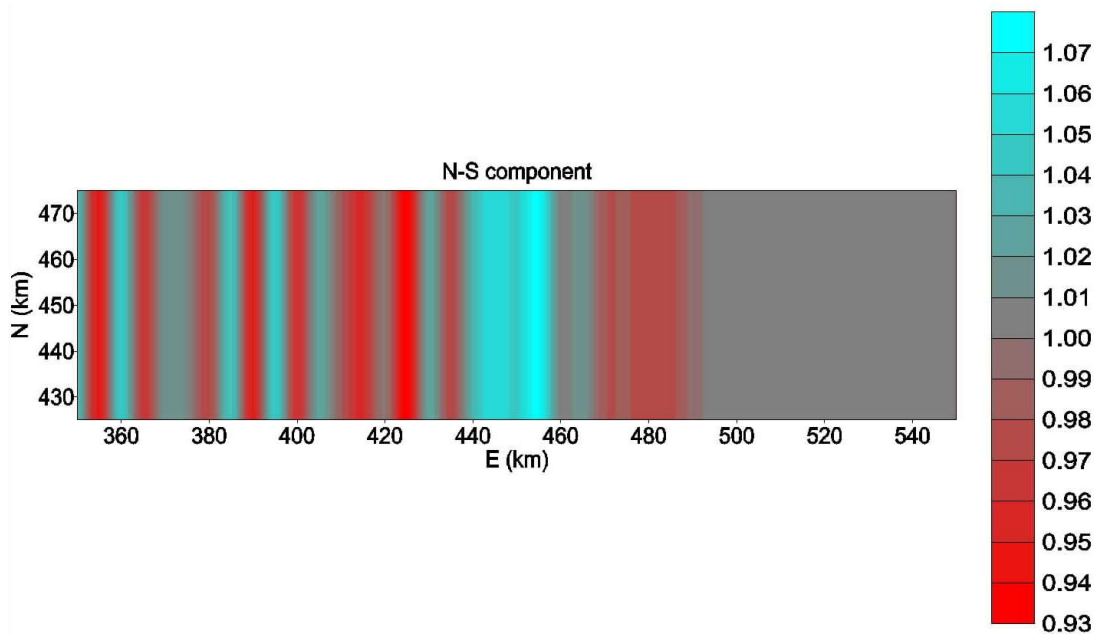
Figure 7. Love surface wave (N-S or tangential component) displacements are shown upon teleseismic fundamental mode Love surface wave arrival from the west onto the structure given in Figure 5 (Love surface wave scattering results).

three obstacles. From this it is straightforward to predict that Rayleigh surface waves observed on the vertical component rather than the horizontal component will perform better when one wishes to study the surface waves for inter-station phase velocity analysis (Yao et al., 2006).

The scattering results due to the incident fundamental mode Love surface waves are shown in Figure 7. Again the spectral amplitudes are illustrated after normalization with respect to the reference medium amplitudes. Similar to the horizontally polarized Rayleigh surface waves in Figure 6, the Love surface waves are also blocked by the three obstacles. Most of the Love surface wave energy is back scattered and is trapped within the obstacles. Only a fraction of the Love surface wave energy continues passing through the obstacles. The latter suggests that the observed Love surface waves analyzed for inter-station phase velocities requires extra attention.

DISCUSSION AND CONCLUSIONS

The resolution power of the teleseismic surface waves is generally limited to those structures called *target anomaly* in Figure 1. The ones called *small anomaly* in the same figure may not be resolved well because the teleseismic surface waves are mostly made of lower frequency fundamental mode propagation. A few higher modes with higher frequency cutoff are also available, but generally smaller in amplitude compared to the fundamental mode because of relatively higher attenuation. In addition, the

higher mode amplitudes are partitioned between broader depth ranges resulting smaller near-surface amplitudes (Kobayashi, 2007).

If the number of data points obtained after discretization and the number of iterative solutions (GMRES; Saad, 2003) applied to the linear system in (18) are given by N and q, respectively, then the overall time complexity can be given as $O(qN \log N)$, which is much more competent compared to, for instance, a direct integration method via the trapezoidal rule with a cost awkward $O(qN^2)$.

The proposed algorithm is able to compute the displacement field for complex structures of arbitrary shapes and sizes within large spatial domains. All three parts illustrated in Figure 2 consume significant amount of computational time where the second part is significantly accelerated by the application of MLFMM. The first and third parts include features suitable for vector or parallel strategies that can be employed to further accelerate the computations.

The 2.5-D treatment is adequate for certain geological structures; e.g. active and passive continental margins, suture zones, mountain ranges and sedimentary valleys. The current study provides a fast algorithm to forward model 2.5-D teleseismic surface wave amplitudes over these structures and is suitable for designing an inversion scheme to solve approximately 2-D velocity structures under linear (or quasi-linear) station arrays. The 2.5-D approximation may not be valid for the propagating medium under the station array, but can be used as initial

models for the complex 3-D studies to reduce the overall cost.

ACKNOWLEDGEMENTS

REFERENCES

Abo-Zena A (1979). Dispersion function computations for unlimited frequency values. Geophys. J. R. Astr. Soc. 58:91-105.

Aki K, Richards PG (1980). Quantitative Seismology:Theory and Methods, ed. Freeman, W.H., San Francisco, CA.

Berteussen KA (1977). Moho depth determinations based on spectral analysis of NORSAR long period P waves. Phys. Earth. Planet Inter. 134:13-27.

Bostock MG (2002). Kirchhoff-approximate inversion of teleseismic wavefields. Geophys. J. Int. 149:787-795.

Bostock MG, Rondenay S, Shragge J (2001). Multiparameter two-dimensional inversion of scattered teleseismic body waves, 1:Theory for oblique incidence. J. Geophys. Res. 106:30771-30782.

Chaillat S, Bonnet M, Semblat JF (2009). A new fast multi-domain BEM to model seismic wave propagation and amplification in 3-D geological Structures. Geophys. J. Int. 177:509-531.

Chaillat S, Bonnet M, Semblat JF (2008). A multi-level fast multipole BEM for 3-D elastodynamics in the frequency domain. Comput. Methods Appl. Mech. Eng. 197:4233-4249.

Chen L, Wen L, Zheng T (2005). A wave equation migration method for receiver function imaging, 2:application to the Japan subduction zone. J. Geophys. Res. 110:B11310, doi:10.1029/2005JB003666.

Chen X (1993). A systematic and efficient method of computing normal modes for multilayered half-space. Geophys. J. Int. 115:391-409.

Cummins PR, Takeuchi N, Geller RJ (1997). Computation of complete synthetic seismograms for laterally heterogeneous models using the Direct Solution Method. Geophys. J. Int. 130:1-16.

Çakir Ö (2008). Simulation of 3-D Teleseismic SV-waves Accelerated by the Multilevel Fast Multipole Method. Pure Appl. Geophys. 165:1707-1732.

Çakir Ö (2006). The multilevel fast multipole method for forward modelling the multiply scattered seismic surface waves. Geophys. J. Int. 167:663-678.

Faccioli E, Maggio F, Paolucci R, Quarteroni A (1997). 2D and 3D elastic wave propagation by a pseudo-spectral domain decomposition method. J. Seismol. 1:237-251.

Fu LY, Bouchon M (2004). Discrete wavenumber solutions to numerical wave propagation in piecewise heterogeneous media, I:theory of two-dimensional SH case. Geophys. J. Int. 157:481-498.

Fujiwara H (2000). The fast multipole method for solving integral equations of three-dimensional topography and basin problems. Geophys. J. Int. 140:198-210.

Fujiwara H (1998). The fast multipole method for integral equations of seismic scattering problems. Geophys. J. Int. 133:773-782.

Gao H, Zhang J (2006). Parallel 3-D simulation of seismic wave propagation in heterogeneous anisotropic media:a grid method approach. Geophys. J. Int. 165:875-888.

Greengard L, Rokhlin V (1987). A Fast algorithm for particle simulations. J. Comp. Phys. 73:280-292.

Gumerov NA, Duraiswami R, Borovikov EA (2003). Data structures, optimal choice of parameters, and complexity results for generalized multilevel fast multipole methods in d dimensions. Computer Science Technical Report No. 4458, Vol. 91, University of Maryland, College Park, Maryland.

Haines AJ, Hulme T, Yu J (2004). General elastic wave scattering problems using an impedance operator approach, I:mathematical development. Geophys. J. Int. 159:643-657.

Huang LJ, Fehler MC (2000). Quasi-Born Fourier migration. Geophys. J. Int. 140:521-534.

Kobayashi N (2007). A new method to calculate normal modes. Geophys. J. Int. 168:315-331.

Laigle M, Becel A, De Voogd B, Hirn A, Taymaz T, Ozalaybey S, Members of SEISMARMARA Leg1 Team (2008). A first deep seismic survey in the Sea of Marmara: Deep basins and whole crust architecture and evolution. Earth Planet. Sci. Lett. 270:168-179.

Lebedev S, Van der Hilst RD (2008). Global upper-mantle tomography with the automated multimode inversion of surface and S-wave forms. Geophys. J. Int. 173:505-518.

Liu E, Zhang Z, Yue J, Dobson A (2008). Boundary integral modelling of elastic wave propagation in multi-layered 2D media with irregular interfaces. Commun. Comput. Phys. 3:52-62.

Lu L, Maupin V, Zeng R, Ding Z (2008). Scattering of surface waves modelled by the integral equation method. Geophys. J. Int. 174:857-872.

Maupin V (2001). A multiple-scattering scheme for modelling surface wave propagation in isotropic and anisotropic three-dimensional structures. Geophys. J. Int. 146:332-348.

Moczo P, Kristek J, Halada L (2000). 3D Fourth-Order Staggered-Grid Finite-Difference Schemes:Stability and Grid Dispersion. Bull. Seism. Soc. Am. 90:587-603.

Nishimura N (2002). Fast multipole accelerated boundary integral equation methods. Appl. Mech. Rev. 55:299-324.

Pain CC, Saunders JH, Worthington MH, Singer JM, Stuart-Bruges W, Mason G, Goddard A (2005). A mixed finite-element method for solving the poroelastic Biot equations with electrokinetic coupling. Geophys. J. Int. 160:592-608.

Papageorgiou AS, Pei D (1998). A Discrete Wavenumber boundary element method for study of the 3-D response 2-D scatterers. Earthq. Eng. Struct. Dyn. 27:619-638.

Pollitz FF (2002). Regional seismic wavefield computation on a 3-D heterogeneous earth model by means of coupled travelling wave synthesis. Pure Appl. Geophys. 159:2085-2112.

Rokhlin V (1985). Rapid solution of integral equations of classical potential theory. J. Comp. Phys. 60:187-207.

Saad Y (2003). Iterative Methods for Sparse Linear Systems, 2nd edn, Society for Industrial and Applied Mathematics, Philadelphia.

Schwab FA, Knopoff L (1972). Fast surface wave and free mode computations, in Methods of Computational Physics Academic Press, New York. 11:87-180.

Schmid C, Van der Lee S, VanDecar JC, Engdahl ER, Giardini D (2008). Three-dimensional S velocity of the mantle in the Africa-Eurasia plate boundary region from phase arrival times and regional waveforms. J. Geophys. Res. 113:B03306, doi:10.1029/2005JB004193.

Snieder R (2002). General theory of elastic wave scattering, Scattering and Inverse Scattering in Pure and Applied Science, pp. 528-542, eds Pike, R. and Sabatier, P., Academic Press, San Diego.

Takeuchi H, Saito K (1972). Seismic surface waves, Methods of computational physics, Academic Press, New York. 11:217-295.

Tromp J, Komatitsch D, Liu Q (2008). Spectral-element and adjoint methods in Seismology. Commun. Comput. Phys. 3:1-32.

Wenzel F, Stenzel KJ, Zimmermann U (1990). Wave propagation in laterally heterogeneous layered media. Geophys. J. Int. 103:675-684.

Wilson D, Aster R, Ni J, Grand S, West W, Gao W, Baldridge WS, Semken S (2005). Imaging the seismic structure of the crust and upper mantle beneath the Great Plains, Rio Grande Rift, and Colorado Plateau using receiver functions. J. Geophys. Res. 110:B05306, doi:10.1029/2004JB003492.

Wu RS, Jin S, Xie XB (2000). Seismic wave propagation and scattering in heterogeneous crustal waveguides using screen propagators, I:SH waves. Bull. Seism. Soc. Am. 90:401-413.

Xia J, Miller RD, Park CB (1999). Estimation of near-surface shear-wave velocity by inversion of Rayleigh waves. Geophysics 64:691-700.

Xu L, Rondenay S, Van der Hilst RD (2007). Structure of the crust beneath the southeastern Tibetan Plateau from teleseismic receiver

functions. Phys. Earth Planet. Int. 165:176-193.

Yamauchi M, Hirahara K, Shibutani T (2003). High resolution receiver function imaging of the seismic velocity discontinuities in the crust and the uppermost mantle beneath southwest Japan. Earth Planet Space 55:59-64.

Yao H, Van der Hilst RD, de Hoop MV (2006). Surface-wave array tomography in SE Tibet from ambient seismic noise and two-station analysis—I. Phase velocity maps. Geophys. J. Int. 166:732-744.

Zhu L (2000). Crustal structure across the San Andreas Fault, southern California from teleseismic converted waves. Earth Planet. Sci. Lett. 179:183-190.